nature communications



Article

https://doi.org/10.1038/s41467-025-60280-9

The nuclear charge radius of 13C

Received: 19 November 2024

Accepted: 15 May 2025

Published online: 07 July 2025

Check for updates

Patrick Müller ^{1,5} ⊠, Matthias Heinz ^{1,2,3,6}, Phillip Imgram ^{1,7}, Kristian König ^{1,4}, Bernhard Maass ^{1,8}, Takayuki Miyagi ^{1,2,3,9}, Wilfried Nörtershäuser ^{1,4} ⊠, Robert Roth ^{1,4} & Achim Schwenk ^{1,2,3}

The size is a key property of a nucleus. Accurate nuclear radii are extracted from elastic electron scattering, laser spectroscopy, and muonic atom spectroscopy. The results are not always compatible, as the proton-radius puzzle has shown most dramatically. Beyond helium, precision data from muonic and electronic sources are scarce in the light-mass region. The stable isotopes of carbon are an exception. We present a laser spectroscopic measurement of the root-mean-square (rms) charge radius of $^{13}{\rm C}$ and compare this with ab initio nuclear structure calculations. Measuring all hyperfine components of the $2\,^3{\rm S} \rightarrow 2\,^3{\rm P}$ fine-structure triplet in $^{13}{\rm C}^{4+}$ ions referenced to a frequency comb allows us to determine its center-of-gravity with accuracy better than 2 MHz although second-order hyperfine-structure effects shift individual lines by several GHz. We improved the uncertainty of $R_{\rm c}(^{13}{\rm C})$ determined with electrons by a factor of 6 and found a 3σ discrepancy with the muonic atom result of similar accuracy.

The main sources for absolute nuclear charge radii of stable isotopes are elastic electron scattering¹ and muonic atom spectroscopy^{2,3}, i.e., the energy determination of X-rays emitted in K_{α} transitions in muonic atoms. The combination of both is considered to deliver the most accurate values, which serve as anchor points for the determination of charge radii along an isotopic chain using isotope-shift measurements in rare and short-lived species^{4,5}. For the proton's size, electronic measurements, i.e., laser spectroscopy of hydrogen⁶ and elastic electron scattering⁷ on one side, and laser spectroscopy of muonic hydrogen on the other side⁸, led to a surprising 7σ discrepancy of the proton's charge radius, which became famously known as the "proton radius puzzle". Even though laser and microwave spectroscopy of ordinary hydrogen become increasingly consistent with the smaller radius from muonic hydrogen⁹⁻¹¹, there are still measurements reporting larger radii^{12,13}. Similarly, the source of the discrepancy in electron scattering is still under debate¹⁴⁻¹⁶ and is a motivation for the MUSE experiment at PSI¹⁷ with the goal to perform muon-proton scattering to test lepton universality in the electromagnetic interaction. Contrary, in 3,4 He, electron scattering and muonic atom laser spectroscopy are in good agreement 18,19 , while the resulting difference in mean-square (ms) charge radius is in tension with several results from laser spectroscopy of ordinary helium 20 . These are, however, affected by a long-standing disagreement—depending on the transition and the applied technique, they scatter by several σ^{21} . Very recently, these tensions in charge radii differences of 3 He and 4 He are partially resolved by taking into account second-order hyperfine corrections 22,23 . For the next elements, Li, Be, and B, nuclear charge radii are about two orders of magnitude less precise than in hydrogen or He and for N, O, and F, it is only slightly better 5,24 . Second-generation muonic X-ray experiments are in preparation that will apply magnetic calorimeters and use improved theoretical calculations to extract absolute nuclear radii of stable isotopes from beryllium to neon 24 .

The only exception in the second row of the periodic table is carbon. The charge radius of 12 C was determined with exceptional 2 and 1 per mille accuracy by electron scattering 25 and muonic atom X-ray spectroscopy 26 , respectively, but a small 2σ discrepancy between

¹Institut für Kernphysik, Technische Universität Darmstadt, Darmstadt, Germany. ²ExtreMe Matter Institute EMMI, GSI Helmholtzzentrum für Schwerionenforschung GmbH, Darmstadt, Germany. ³Max-Planck-Institut für Kernphysik, Heidelberg, Germany. ⁴Helmholtz Research Academy Hesse for FAIR, GSI Helmholtzzentrum für Schwerionenforschung, Darmstadt, Germany. ⁵Present address: Department of Physics and Astronomy, University of California Los Angeles, Los Angeles, CA, USA. ⁶Present address: National Center for Computational Sciences, Oak Ridge National Laboratory, Oak Ridge, TN, USA. ⁷Present address: Instituut voor Kern- en Stralingsfysica, KU Leuven, Leuven, Belgium. ⁸Present address: Physics Division, Argonne National Laboratory, Argonne, IL, USA. ⁹Present address: Center for Computational Sciences, University of Tsukuba, Tsukuba, Japan. □ e-mail: pmueller@physics.ucla.edu; wnoertershaeuser@ikp.tu-darmstadt.de

the two values is observed. For ¹³C, the second stable isotope, results from both methods agree within the comparably large uncertainty of the electron-scattering result. Thus, there is a demand for more precise knowledge of the charge radius of ¹³C from the electronic sector. Moreover, radii of light nuclei are also particularly interesting for nuclear structure theory as they are accessible to different ab initio methods and show substantial structural changes between neighboring isotopes²⁷. A reason for this is the tendency of the nucleons to form α clusters, which in light nuclei constitute a large portion of the nucleus^{28–35}. To reproduce the size of the firmly bound $p_{3/2}$ subshellclosed nucleus of 12C with ab initio nuclear structure calculations, a significant admixture of a 3α -cluster configuration is required that is governed by the 0_2^+ Hoyle state³⁶⁻⁴⁰. This characteristic structure is essential in the 3α -nucleosynthesis process in stars supernovae^{41–43}. In ¹³C, the additional neutron may be thought to act as a covalent bond inside the 3α structure³², explaining the smaller radius of ¹³C compared with ¹²C as it was determined consistently by elastic electron scattering and muonic atom spectroscopy. The experimental accuracy of the 13C radius solely based on electronic measurements can be improved by combining the accurate ¹²C electron scattering result with a precise determination of the differential ms charge radius $\delta \langle r^2 \rangle^{12,13}$ extracted from an isotope-shift measurement.

So far, there is no laser-spectroscopic nuclear structure information for the elements beyond Be^{44,45} up to neon⁴⁶. This holds for the stable and short-lived isotopes except for a measurement of the isotope shift in stable 10,11B35. Efforts in the laser-spectroscopic determination of charge radii in this region have to face three main challenges: Firstly, the electronic level schemes of the elements above boron are complicated, and excitation from the ground state of atoms or singly charged ions is not feasible with currently available high-precision lasers. Secondly, high-accuracy mass-shift calculations for the systems beyond boron, which are required to extract the nuclear charge radius, are unavailable. Finally, due to their chemical reactivity, most of these elements can only be extracted in the form of molecules at online isotope separator facilities, while at in-flight facilities, the stopping of such light products requires large stopping cells and the yields are comparably low. Here, we demonstrate an approach that opens up prospects for such measurements by simultaneously overcoming all three hurdles.

Our experimental method is based on generating He-like ions—in this case, C^{4+} ions—in the excited metastable $1s2s^3S_1$ state. From here, laser excitation into the $1s2p^3P_J$ manifold is possible with ultraviolet light. This transition has been previously studied in $^{12}C^{4+}$ to perform a test of non-relativistic quantum electrodynamics (NRQED) calculations and to demonstrate that an "all-optical" nuclear charge radius extraction with high accuracy is potentially possible 47,48 . While the charge radius of 12 C can, in principle, be extracted directly from the transition frequency, theory is not yet sufficiently advanced to make this "all-optical" approach competitive with the alternative methods 47 . In this work, we present a measurement of the charge radius of 13 C based on an optical isotope-shift measurement and NRQED mass-shift calculations with accuracy that already exceeds the available electron-scattering data on 13 C. Since the isotope shift, i.e., the difference in transition frequency between two isotopes with mass numbers A and A'

$$\delta \nu^{A,A'} = \nu^{A'} - \nu^{A} = \delta \nu^{A,A'}_{M} + F \delta \langle r^2 \rangle^{A,A'}, \qquad (1)$$

it thus follows that the change in the ms nuclear charge radius can be extracted according to

$$\delta \langle r^2 \rangle^{A,A'} = \frac{\delta \nu^{A,A'} - \delta \nu_{\rm M}^{A,A'}}{F} \tag{2}$$

in a nuclear-model independent way, provided that the mass-shift $\delta\nu_{\rm M}$ and the field-shift factor F can be reliably calculated.

This approach is currently only possible for up to five-electron systems ³⁵. Hence, spectroscopy on neutral carbon atoms is not an option, but mass-shift calculations for the He-like system C⁴⁺ are readily available, and the field-shift factor of -211.5(1) MHz/fm² in the laser-accessible 1s2s $^3S_1 \rightarrow 1s2p$ $^3P_{0,1,2}$ transition provides a high sensitivity to the charge radius. Our measurement of the charge radius of 13 C makes the 12,13 C pair the nuclei with the currently best-known nuclear charge radii besides the stable isotopes of hydrogen and helium, for which laser spectroscopy was performed on muonic atoms 18,19,49 . We finally note that this has been achieved despite strong perturbations by hyperfine-induced fine-structure mixing and required high-precision measurements of all nine hyperfine components in the three fine-structure lines.

Results

We performed the measurements at the COllinear Apparatus for Laser Spectroscopy and Applied Sciences (COALA) at the Institute for Nuclear Physics at TU Darmstadt. The setup and the recent extensions for highly charged ions are described in refs. 48,50, and we only briefly summarize the most relevant aspects for our work. A sketch of COALA and the measurement principle is depicted in Fig. 1. A continuous beam of ¹³C⁴⁺ ions with a beam current of approximately 1.5 nA and an energy of 50 keV is produced in our electron-beam ion source (EBIS-A, DREEBIT GmbH). We feed ¹³C-enriched methane gas (¹³CH₄) at a pressure of $6 \cdot 10^{-8}$ mbar into the EBIS. The molecules are cracked and charge states up to fully stripped C6+ ions are reached through subsequent collisions of the ions with the electron beam. The ions are confined by the electrostatic potentials of the trap electrodes and the electron beam's space charge in axial and radial directions, respectively. The starting point for laser spectroscopy is the metastable 1s2s ³S₁ state in He-like ¹³C⁴⁺ with a lifetime of 21 ms⁵¹. It is dominantly populated through electron-capture processes of C^{5+ 48}. The electrode generating the axial trapping potential at the trap exit is only 200 V above the central trap potential (\approx +12.5 kV). Thus, a small fraction of the trapped ions continuously leaks out of the trap and is accelerated toward ground potential. A velocity filter (Wien filter) formed by crossed magnetic and electric fields is used to separate the ¹³C⁴⁺ ions from other charge states and ion species. Behind the source region, an electrostatic 60°-bender, followed by xy-steerers and a quadrupole doublet, is used to superimpose the ion-beam with the laser beams and to shape the ion beam, respectively. The fluorescence detection region (FDR) is floated on a scan voltage $U_{\rm scan}$ to adjust the ion velocity and thereby scan the laser frequency in the rest-frame of the ions (Doppler tuning).

Two continuous-wave Ti:sapphire lasers produce light between 906 and 914 nm that is twice frequency doubled to create the range from 226.5 to 228.5 nm required to perform collinear and anticollinear laser spectroscopy on the $^{13}C^{4+}$ ions in fast alternation. We note that the lines are shifted by ± 0.6 nm due to the Doppler shift. The exact frequency depends on the ion velocity, but this dependency is eliminated if the resonance frequencies in both collinear $\nu_{\rm c}$ and anticollinear $\nu_{\rm a}$ direction are determined. The geometric average $\nu_0 = \sqrt{\nu_a \nu_c}$ of the observed resonance frequencies in the laboratory frame is the transition frequency in the rest frame of the ion. Both Ti:sapphire lasers are simultaneously locked to a frequency comb to obtain $\nu_{\rm a}$ and $\nu_{\rm c}$ with high accuracy.

A schematic of the hyperfine structure in the $1s2s^3S_1 \rightarrow 1s2p^3P_{0,1,2}$ multiplet is shown in Fig. 2a, and the observed spectrum is depicted in (b). The HFS is well resolved in all transitions and spans 60 to 90 GHz. The relative peak heights vary based on their dipole transition strengths, with the peak of the weakest transition being ten times smaller than that of the strongest. Due to the large hyperfine splitting and the narrow full width at half maximum of 150 MHz, the individual transitions are compressed to a line in the overview plot. Therefore, the fits are shown in the inset for the smallest (left) and the strongest (right) hyperfine components to indicate the typical statistical significance. Resonances are fitted with a pure Gaussian lineshape since

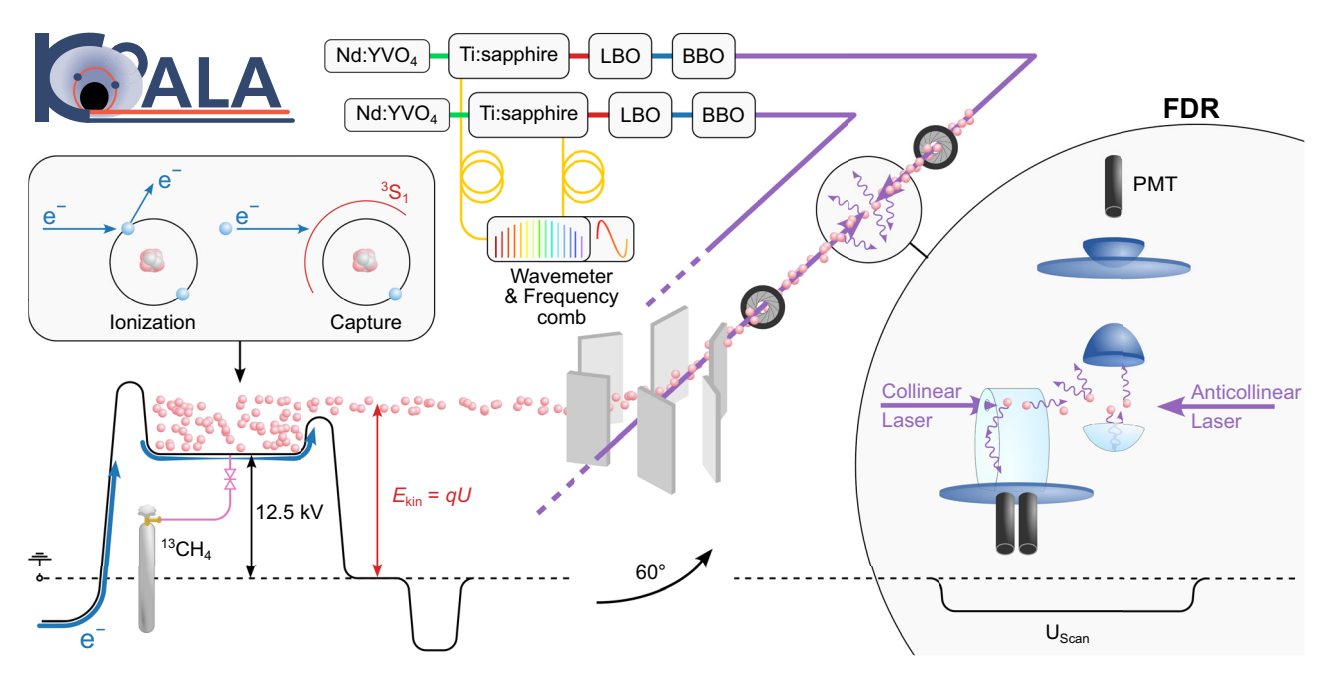


Fig. 1 | **Experimental setup.** Sketch of the measurement principle including the electron-beam ion source (EBIS), the electrostatic switchyard, the beam alignment irises, the laser system, and the fluorescence detection region (FDR). The laser system consists of two Millennia pump lasers (Nd:YVO₄) that drive two Ti:Sapphire lasers, each followed by two frequency doublers, one operated with lithium-

triborate (LBO) and second one with barium betaborate (BBO). The lasers are locked to a wavemeter and a frequency comb. The 227-nm light is then transported through air to the COALA beamline. The two charge-breeding processes, electron-impact ionization and electron capture, are shown in the inset above the EBIS potential.

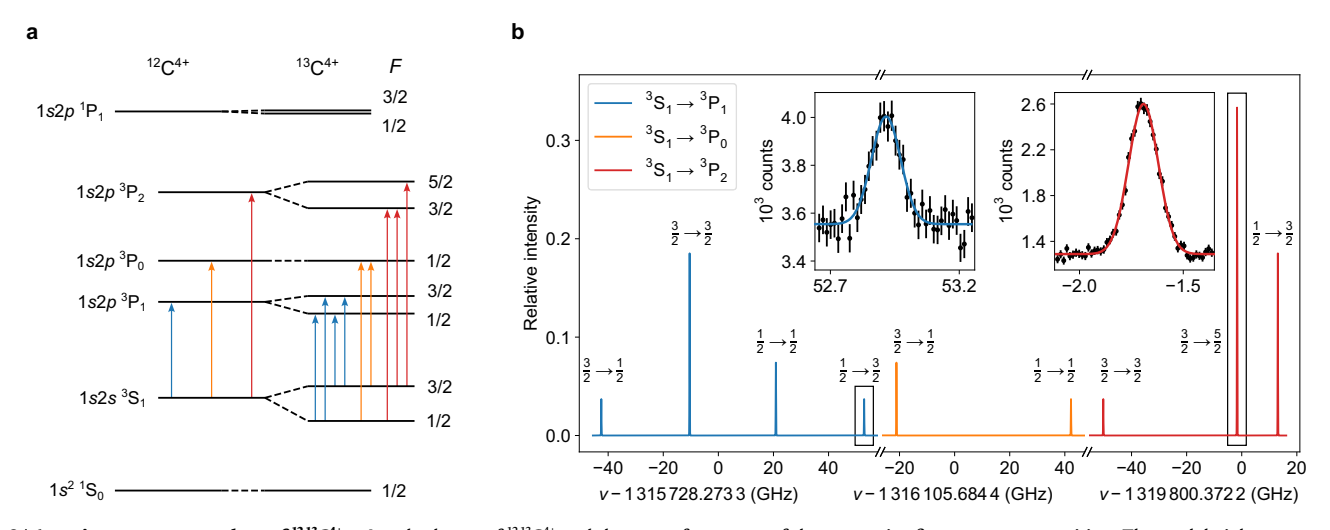


Fig. 2 | **Atomic spectroscopy data of** ^{12,13}C⁴⁺. **a** Level scheme of ^{12,13}C⁴⁺ and the electric dipole transitions that are addressed by the laser. **b** Hyperfine-structure (HFS) spectrum of the 1s2s $^3S_1 \rightarrow 1s2p$ $^3P_{0,1,2}$ transitions in $^{13}C^{4+}$ simulated with the experimentally determined frequencies and linewidths. The *x*-axis represents the laser frequency in the rest-frame of the ion ν relative to the center-of-gravity

frequency of the respective fine-structure transition. The peak heights were set to the theoretical transition strengths used in Eq. (7). The two insets show measured spectra of the marked transitions. Next to the resonances, the contributing quantum numbers $F \to F'$ of the lower and upper states are shown, respectively.

the natural linewidth of 9 MHz⁵¹ and possible homogeneous broadening mechanisms are negligible compared to the width of the velocity distribution of the ions. The total statistical uncertainty of the resonance center is in all cases $\lesssim 1$ MHz and therefore significantly smaller than potential systematic shifts.

The largest systematic uncertainty originates from the imperfect alignment of the two laser beams. If the collinear and the anticollinear laser beams are slightly offset in the detection region, they address different ion velocities and the Doppler shift is not fully canceled in the geometric average. Experimental verification of this effect provided a conservative limit of 1.7 MHz under the given experimental conditions⁴⁸. This is the dominant contribution to the systematic

uncertainty. Adding all systematics in square (beam alignment, Zeeman effect, uncorrected photon recoils) yields a total systematic uncertainty of 1.8 MHz. Due to the linear dependence of the frequency shift on the statistical misalignment of the laser beams and the daily realignment of the ion and laser beams, we expect the dominant systematic uncertainty to fluctuate centered around the atomic transition frequency. Thus, the statistical and systematic uncertainties are added in square to obtain the total uncertainties. For details, see Methods.

The transition frequencies of all hyperfine-structure lines are compiled in Table 1. The individual transition frequencies of ¹²C⁴⁺ from ref. 47 and the center-of-gravity (cg) frequency of the fine-structure multiplet are also included. For each fine-structure component of ¹³C,

Table 1 | Electronic transition frequencies ν^{13} and isotope shifts $\delta \nu^{12,13}$ of the 1s2s³S_{(J,F)'} $F \rightarrow 1$ s2p³P_{(J,F)'} transitions in ¹³C⁴⁺

$(\mathbf{J},\mathbf{F}) o (\mathbf{J}',\mathbf{F}')$	$\nu_{(\mathbf{J},\mathbf{F})\to(\mathbf{J}',\mathbf{F}')}^{13}$	δν <mark>12,13</mark>
$(1, 1/2) \rightarrow (0, 1/2)$	1 316 147 920.6 (1.9)	_
$(1, 3/2) \rightarrow (0, 1/2)$	1 316 084 566.3 (1.8)	_
$1 \to \tilde{0}$	1 316 105 684.4 (1.4)	53 465.1 (2.3)
1 → 0	1 316 103 946.9 (1.3)	51727.6 (2.3)
$1 \rightarrow 0$, ${}^{12}C^{4+47}$	1 316 052 219.3 (1.9)	_
(1, 1/2) → (1, 1/2)	1 315 749 143.7 (1.9)	_
(1, 1/2) → (1, 3/2)	1 315 781 189.1 (2.0)	_
(1, 3/2) → (1, 1/2)	1 315 685 791.2 (2.0)	_
(1, 3/2) → (1, 3/2)	1 315 717 838.5 (1.8)	_
$1 \rightarrow \tilde{1}$	1 315 728 273.3 (1.1)	51 080.5 (2.0)
1 → 1	1 315 728 925.4 (1.0)	51732.6 (2.0)
$1 \rightarrow 1$, $^{12}C^{4+47}$	1 315 677 192.8 (1.7)	_
(1, 1/2) → (2, 3/2)	1 319 813 468.4 (1.8)	_
(1, 3/2) → (2, 3/2)	1 319 750 116.8 (1.8)	_
(1, 3/2) → (2, 5/2)	1 319 798 680.5 (1.8)	_
$1 \to \tilde{2}$	1 319 800 372.2 (1.2)	51 800.8 (2.1)
1 → 2	1 319 800 329.2 (1.2)	51 757.8 (2.1)
$1 \rightarrow 2$, ${}^{12}C^{4+47}$	1 319 748 571.4 (1.7)	_
$S \to \tilde{P}$	1 318 032 485.0 (0.8)	51745.6 (1.4)
$S \rightarrow P$	1 318 032 485.5 (0.8)	51746.1(1.4)
$S \rightarrow P$, $^{12}C^{4+}$	1 317 980 739.4 (1.1)	_

The center-of-gravity (cg) frequencies below the individual resonance frequencies are calculated using Eqs. (7) and (8), with and without hyperfine-induced mixing considered, respectively. The isotope shifts in the third column are the differences between the absolute transition frequencies in this table and the results in ¹²C^{4+ 47}. All values are given in MHz.

the hyperfine cg was first obtained assuming the usual first-order hyperfine structure splitting (for details, see Methods) and is listed in the table indicated as $1 \rightarrow \tilde{J}$. A look at the individual isotope shifts relative to the corresponding fine-structure transition in ¹²C shows that these vary over 2.4 GHz even though they are expected to be equal. Second-order effects cause this discrepancy, i.e., the mixing of hyperfine states with the same quantum number *F* belonging to different fine-structure levels. Including second-order HFS explicitly, using the theoretical magnetic dipole matrix elements tabulated in ref. 52 (see Methods), we obtain the cg as provided in the table indicated by $1 \rightarrow J$. In this case, the isotope shift of all three fine-structure components agree to ≤30 MHz, demonstrating that the calculated magnetic properties capture the shifts induced by state mixing well. We attribute the remaining difference to the "splitting isotope shift" that provides an important benchmark for NRQED calculations⁵³. The comparison between the values obtained with and without hyperfine mixing reveals that the shifts of the ${}^{3}P_{0.1}$ levels are much larger than the shift of the more separated ${}^{3}P_{2}$ level.

The isotope shifts of the ${}^3S_1 \rightarrow {}^3P_J$ fine-structure centroid determined by the two approaches differ by only 500 kHz. This difference is ascribed to the small contribution of the well-separated 1P_1 level. The excellent agreement, much smaller than our uncertainty, demonstrates that measuring all hyperfine components is a reliable way to circumvent the impact of hyperfine mixing and to extract the charge radius with high accuracy, which is particularly important for upcoming measurements on B^{3+} .

The differential ms nuclear charge radius $\delta\langle r^2\rangle^{12,13}$ is determined from the isotope shift of the cg frequency of the entire fine structure using Eq. (2) and (7). The required NRQED atomic structure calculations of the mass-shift contribution $\delta v_{\rm M} = 51\,719.29(25)$ MHz and the field-shift constant F = -211.5(1) MHz/fm² were carried out by Yerokhin et al. up to the order of $m\alpha^6$ 54. The finite-nuclear-size effect in the isotope shift is the difference between our experimental value and the

calculated mass-shift contribution. It amounts to only 26.3(1.4) MHz, which is a 2×10^{-8} fraction of the transition frequency. From the results described above, we derive a differential nuclear charge radius of

$$\delta \langle r^2 \rangle^{12,13} = -0.1245(66) \,\text{fm}^2$$
 (3)

$$\delta R_c^{12,13} = -0.0253(14) \,\text{fm}.$$
 (4)

Our results for the rms charge radii of ¹³C and the change in rms charge radii are plotted in Fig. 3 and compared to results from electron scattering and muonic atom X-ray spectroscopy. The numerical values are included in Table 2. For 12C, the most accurate muonic measurement by Ruckstuhl et al.²⁶ disagrees with the weighted average of all electron-scattering results by about 2.4 σ of the combined uncertainty. Combining the e⁻-scattering charge radius of ¹²C with the ^{12,13}C⁴⁺ isotope-shift measurement provides a charge radius for ¹³C that is in excellent agreement with the result of the ¹³C e⁻-scattering⁵⁵ but has 6 times reduced uncertainty, which is now similar to the uncertainty of the muonic atom result⁵⁶. The discrepancy in terms of the combined uncertainty is even slightly larger than in 12 C (2.8 σ compared to 2.4 σ). $\delta \langle r^2 \rangle^{12,13}$ obtained from the difference in the muonic radii is smaller and has three times larger uncertainty than the laser-spectroscopic result, and just agrees within the combined uncertainty. Thus, we find a systematic offset in radii based on electromagnetic interaction with electrons versus those with muons. This is a different situation as in the α -helion discrepancy, since the charge radius difference measured in ordinary ions agrees with that observed in muonic atoms, but the absolute charge radius from electron scattering does not. In the past, ¹²C was always considered an excellent reference for charge radii measurements due to the high accuracy of the e-scattering result. This calls for verifying the e⁻-scattering and the muonic atom results.

Discussion

From a theoretical point of view, the carbon isotopes, especially ¹²C. due to their pronounced cluster structure, have long been theoretically interesting and challenging to describe via ab initio methods. Early explorations within the framework of fermionic molecular dynamics provided a quantitative description of various structures of ¹²C, including the Hoyle state, albeit with necessary phenomenological tuning of the interaction to a broad range of nuclear structure properties⁵⁷⁻⁵⁹. More recent lattice simulations based on nuclear interactions from chiral effective field theory (EFT) predicted the structure of the ground and Hoyle state of ¹²C without adjustment based on the natural description of α -clustering in such simulations ^{38,60,61}. Over the past 15 years, ab initio calculations of nuclei as heavy as ²⁰⁸Pb have been performed using systematically improvable many-body methods⁶²⁻⁶⁴ like the in-medium similarity renormalization group (IMSRG)⁶⁵. Early IMSRG studies that included calculations of ¹²C found atypically large differences in ground-state energies predicted by different approaches, indicating that the manybody description of ¹²C is challenging⁶⁶⁻⁶⁸. New experimental measurements and theoretical predictions of ¹²C and ¹³C provide an interesting avenue to study not only the changing structure of carbon isotopes, but also how it emerges from nuclear forces and many-body methods.

We predict the properties of ^{12,13}C using ab initio valence-space IMSRG (VS-IMSRG)⁶⁷ and in-medium no-core shell-model (IM-NCSM)⁶⁸ nuclear structure calculations, which solve the many-body Schrödinger equation for a given input nuclear Hamiltonian in an approximate, but systematically improvable manner. We employ Hamiltonians with nucleon-nucleon and three-nucleon interactions from chiral EFT, using seven Hamiltonians that differ in their construction and how they are fitted to data to give insight into interaction uncertainties. VS-IMSRG(2) calculations were performed using 1.8/

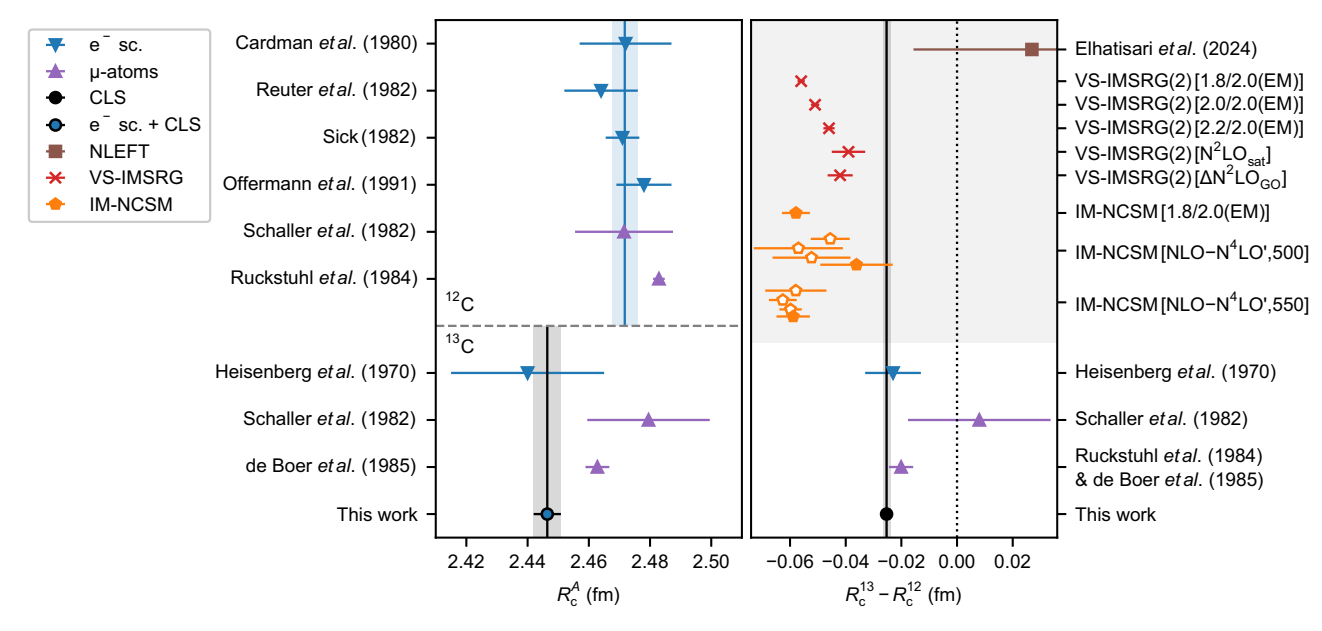


Fig. 3 | **Absolute and differential nuclear charge radii of** ^{12,13}**C.** Experimentally determined absolute $R_{\rm c}^{12}$, $R_{\rm c}^{13}$ and nuclear charge radius difference $\delta R_{\rm c}^{12,13} = R_{\rm c}^{13} = R_{\rm c}^{13} = R_{\rm c}^{12}$ of ^{12,13}C determined with elastic electron scattering (blue), muonic atom spectroscopy (μ -atoms, purple) and collinear laser spectroscopy (CLS, black). Results from CLS and e⁻-scattering were combined to obtain an improved $R_{\rm c}^{13}$ (black & blue) purely from electronic measurements. The differential rms nuclear charge radii from e⁻-scattering and μ -atoms are differences of absolute radii while the CLS result

is determined directly from the isotope shift and ab initio atomic structure calculations using Eq. (2). $\delta R_{\rm c}^{12.13}$ is also compared to ab initio valence-space in-medium similarity renormalization group (VS-IMSRG, red) and in-medium no-core shell-model (IM-NSCM, orange) calculations. The lower-order IM-NSCM results are plotted with open symbols. Results from nuclear-lattice effective field theory (NLEFT, brown) were published by Elhatisari et al. ⁶¹. The numerical values of this plot are listed in Table 2.

Table 2 | Absolute and differential nuclear charge radii of ^{12,13}C determined with different ab initio nuclear structure calculations and experiments

Method	-12	_ 10	-12 -12
	R _c ¹²	R _c ¹³	$R_{\rm c}^{13} - R_{\rm c}^{12}$
NLEFT [N³LO] ⁶¹	2.490(12)	2.521(41)	0.027(43)
VS-IMSRG(2) [1.8/2.0(EM)]	2.416(1)	2.361(1)	-0.056(1)
VS-IMSRG(2) [2.0/2.0(EM)]	2.421(1)	2.370(1)	-0.051(2)
VS-IMSRG(2) [2.2/2.O(EM)]	2.423(1)	2.377(1)	-0.046(2)
VS-IMSRG(2) [N ² LO _{sat}]	2.405(1)	2.366(6)	-0.039(6)
VS-IMSRG(2) $[\Delta N^2 LO_{GO}]$	2.396(3)	2.354(2)	-0.042(5)
IM-NCSM [1.8/2.0(EM)]	2.421(16)	2.363(12)	-0.058(5)
IM-NCSM [NLO, 500]	2.348(249)	2.302(248)	-0.046(7)
IM-NCSM [N ² LO, 500]	2.521(103)	2.464(101)	-0.057(16)
IM-NCSM [N ³ LO, 500]	2.532(38)	2.479(27)	-0.052(14)
IM-NCSM [N ⁴ LO', 500]	2.550(13)	2.513(20)	-0.036(13)
IM-NCSM [NLO, 550]	2.471(239)	2.413(229)	-0.058(11)
IM-NCSM [N ² LO, 550]	2.426(63)	2.364(62)	-0.063(5)
IM-NCSM [N ³ LO, 550]	2.457(31)	2.397(30)	-0.060(4)
IM-NCSM [N ⁴ LO', 550]	2.482(23)	2.423(20)	-0.059(6)
e ⁻ -scattering ^{25,55,90-92}	2.4717(42)	2.440(25)	-0.023(10)
μ-atom ⁹³	2.472(16)	2.480(20)	0.008(26)
μ-atom ^{26,56}	2.4829(19)	2.4628(39)	-0.0201(43)
CLS [this work]	_	2.4464(45)	-0.0253(14)

The maximum employed many-body orders or interactions of the theory results are given in square brackets. Radii are given in fm.

2.0(EM), 2.0/2.0(EM), $2.2/2.0(EM)^{69}$, $N^2LO_{sat}^{70}$, and $\Delta N^2LO_{GO}^{71}$, while for IM-NCSM calculations a family of non-local interactions up to N^4LO' was employed $N^2LO_{Sat}^{70}$. We confirm the consistency of the two approaches by comparing VS-IMSRG(2) and IM-NCSM calculations with the 1.8/2.0(EM) Hamiltonian. More details on the Hamiltonians, methods and charge radii calculations are provided in Table 2 and Methods. Here, we concentrate on the results for the charge radii difference between the isotopes, which are shown in the right part of Fig. 3 and are compared with the experimental results. A plot of the absolute nuclear charge radii is shown in Fig. 4.

The experimentally observed size reduction of 0.0253(14) fm is overestimated by up to a factor of 2 in our calculations. The closest results are obtained with the VS-IMSRG using N²LO_{sat} and the IM-NCSM calculations with the N⁴LO'(500) interactions. We note that the VS-IMSRG(2) calculations have uncertainties that are estimated solely from the model-space convergence. The uncertainties of the IM-NCSM calculations additionally include the Hamiltonian uncertainty and the convergence of the many-body expansion, with the exception of the 1.8/2.0(EM) Hamiltonian where only the many-body uncertainty is quantified. Thus, the scatter of the VS-IMSRG results beyond uncertainties is not unexpected. The VS-IMSRG(2) calculations underestimate the absolute charge radii for all Hamiltonians, suggesting a systematic underprediction due to the VS-IMSRG(2) approximation. VS-IMSRG(3) calculations were performed with the 1.8/2.0(EM) interaction to investigate the many-body uncertainty⁷³. This brings the absolute radii in better agreement with the experiment, but further increases the discrepancy from the observed $\delta R_c^{12,13}$ by almost a factor of 2.

The IM-NCSM calculations in Table 2 show interesting dependencies of the charge radii, increasing with chiral order and decreasing with higher cutoff scale. For 550 MeV/c we find good agreement with the muonic atom experiment for the charge radii of both isotopes at

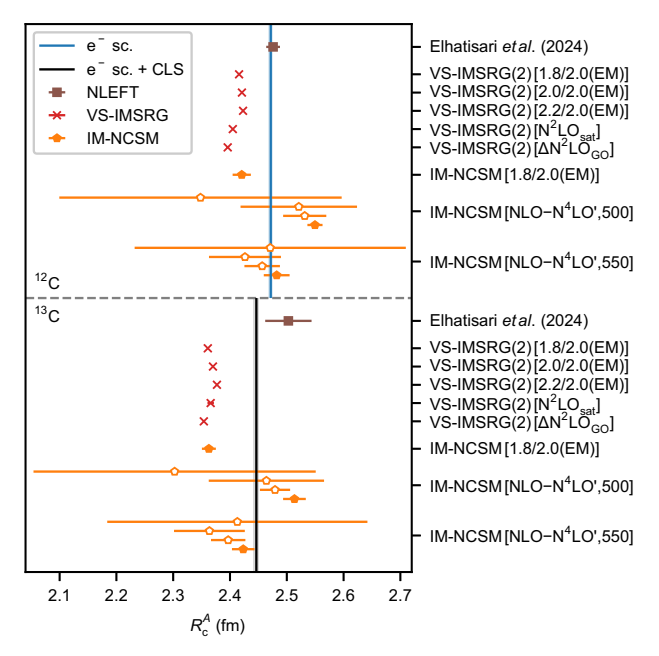


Fig. 4 | **Theoretical absolute nuclear charge radii of** 12,13 **C.** The radii $R_{\rm c}^{12,13}$ have been determined from ab initio valence-space in-medium similarity renormalization group (VS-IMSRG, red) and in-medium no-core shell model (IM-NSCM, orange) calculations. The lower-order IM-NSCM results are plotted with open symbols. Results from nuclear-lattice effective field theory (NLEFT, brown) were published by Elhatisari et al.⁶¹. The numerical values of this plot are listed in Table 2.

N⁴LO′, but for the radius difference, the situation is reversed, providing a value compatible with experiment for cutoff 500 MeV/*c*. At N²LO and N³LO, however, both cutoffs provide a similar radius difference, pointing more towards the overestimated value.

We highlight that the theoretical prediction of the charge radius difference $\delta R_{\rm c}^{12,13}$ benefits from the cancellation of correlated systematic uncertainties in the predictions of the absolute charge radii $R_{\rm c}^{12}$ and $R_{\rm c}^{13}$. This is clearly visible in the uncertainties of our IM-NCSM calculations, where Hamiltonian and many-body convergence uncertainties are quantified. To quantify these uncertainties for $\delta R_{\rm c}^{12,13}$, we apply a Bayesian uncertainty quantification protocol (based on ref. 74 and described in Methods) directly to the charge radius difference, implicitly accounting for the cancellation of correlated uncertainties. As a result, the charge radius difference uncertainty is typically smaller than that of the absolute charge radii and also smaller than the resulting uncertainty if the uncertainties on $R_{\rm c}^{12}$ and $R_{\rm c}^{13}$ were uncorrelated.

All our ab initio calculations consistently predict a negative charge radius difference. The underprediction by both methods for all Hamiltonians, however, suggests that some relevant many-body correlations necessary for the precise prediction of this small difference are missing, requiring the development of improved many-body approximations to resolve.

The systematic discrepancy between the charge radii obtained in ^{12,13}C using electron or muon interactions, uncovered by our measurements, must be consolidated or resolved by improved measurements on muonic atoms that are currently prepared by the QUARTET collaboration²⁴. Laser spectroscopy of ¹⁴C is currently ongoing at COALA and will provide the nuclear charge radius of this isotope with comparable precision as obtained here for ¹³C and thus improve it by more than an order of magnitude compared to previous measurements.

Methods

Determination of the isotope shift

The absolute transition frequencies v_i used in Eq. (7) are determined using frequency comb-referenced quasi-simultaneous collinear (c) and

anticollinear (a) laser spectroscopy. Fluorescence spectra are typically taken with 61 steps across a span of 800 MHz. All recorded spectra were fitted using the least-square algorithm optimize.leastsq provided by the scipy Python package⁷⁵. A pure Gaussian model

$$g(\nu, \nu_{c/a}, \sigma, a, b) = a + b \exp\left[-\frac{(\nu - \nu_{c/a})^2}{2\sigma^2}\right]$$
 (5)

was used to fit the data, since the natural linewidths of 9 MHz⁵¹ of the transitions are negligible compared with the width of the velocity distribution of the ions. The typical full width at half maximum of a resonance is 150 MHz. The resonance centers ν_a and ν_c obtained from the corresponding anticollinear and collinear spectra, respectively, are combined to calculate the rest-frame frequency

$$\nu_0 = \sqrt{\nu_c \nu_a} - \frac{h \nu_c \nu_a}{2mc^2}.$$
 (6)

The small second term, which amounts to 0.3 MHz for $^{13}C^{4+}$, takes care of the photon-recoil contribution that is transferred into kinetic energy of the ion during absorption. At least 28 anticollinear-collinear (ac) or collinear-anticollinear (ca) measurement pairs were taken for each hyperfine transition to minimize statistical fluctuations, and in all cases, the standard deviation of the mean was $\lesssim 1\,\mathrm{MHz}$.

There is some freedom in the choice of the isotope shift $\delta \nu^{A,A'}$ as it can be defined as any difference of linear combinations of transition frequencies sensitive to the nuclear charge radius. To get the smallest possible uncertainty, we calculate the weighted mean of all (hyper) fine-structure transition frequencies $\nu_i \in 1s2s\,^3S_1 \to 1s2p\,^3P_{0,1,2}$ for $^{12,13}C$. The weights are the theoretical transition strengths assuming no hyperfine-induced mixing. The cg frequency of the $^3S_1 \to ^3P_J$ multiplet for each isotope is calculated as

$$\nu^{A} = \sum_{i} \nu_{i} \frac{(2F+1)(2F'+1)(2J'+1)}{3(2J+1)(2J+1)} \begin{cases} J' & J & 1 \\ F & F' & I \end{cases}^{2}, \tag{7}$$

where J,J' and F,F' are the electronic and total angular momentum quantum numbers of lower and upper state, respectively, and I is the nuclear spin. This weighted mean is insensitive to hyperfine-induced mixing between the 1s2p $^3P_{0,1,2}$ states and gives the same result as fitting the standard formula for HFS splittings to the resonance frequencies. In a second analysis, we have considered hyperfine-induced mixing explicitly, applying the theoretical magnetic dipole matrix elements $\langle \gamma'J'||T^{(1)}||\gamma''J''|\rangle$ tabulated in ref. 52. By fitting

$$\nu_{(J,F)\to(\gamma'\bar{J},F')} = \nu_{J\to(\gamma'\bar{J},F')} - \frac{A_J}{2} [F(F+1) - J(J+1) - I(I+1)]$$
 (8)

to the resonance frequencies, where $\nu_{J\to (\gamma\bar{J},F')}$ are the eigenvalues of the matrices with the entries 52

$$\begin{split} \Omega_{(\gamma'J')(\gamma''J'')}^{F'} &= \nu_{J \to (\gamma'J')} \delta_{(\gamma'J')(\gamma''J'')} \\ &+ (-1)^{I+J'+F'} \left\{ \begin{matrix} I & J' & F' \\ J'' & I & 1 \end{matrix} \right\} \sqrt{\frac{(2I+1)(I+1)}{I}} \mu_I \left\langle \gamma'J' || T^{(1)} || \gamma''J'' \right\rangle, \end{split}$$

hypothetical cg frequencies $\nu_{J\to (\gamma'f')}$ can be extracted that would result from Eq. (7) if there was no mixing between different J' states. Here \tilde{J} is a label for the experimentally accessible mixed-J states, A_J is the HFS constant of the magnetic dipole contribution to the energy of the 3S_1 state, $\delta_{(\gamma'f')(\gamma'f'')}$ is the Kronecker delta, $\{:::\}$ is the Wigner-6j symbol, $\mu_I = 0.702\,369\,(4)\,\mu_N^{\,76}$ is the magnetic dipole moment of the nucleus and $\gamma' = 2S' + 1$ is the spin multiplicity of the state $^{\gamma}P_{J'}$. In the fit of Eq. (8) to the resonance frequencies, A_J , $\nu_{J\to (\gamma'f')}$ and the diagonal elements

 $\langle 3J'||T^{(1)}||3J'\rangle$ are taken as free parameters. Mixing with the $1s2p^{1}P_{1}$ state was taken into account using a fixed $\nu_{1\rightarrow 11}$ and $\langle 11||T^{(1)}||11\rangle$. This procedure relies on the calculated off-diagonal matrix elements $\langle yJ'||T^{(1)}||yJ''\rangle$, for which no uncertainty is specified in ref. 52. Assuming a relative uncertainty of 10^{-4} for the matrix elements of $T^{(1)}$, which are specified to five significant digits, yields shifts of the cg frequencies of ≤ 0.5 MHz, and are, thus, considerably smaller than the experimental uncertainty. The combined cg frequency of all ${}^3S_1 \rightarrow {}^3P_{0.1.2}$ transitions is additionally affected by mixing with the 1s2p P₁ level. This contribution is expected to be small due to its large distance in energy from the ³P levels. It can be estimated from the difference between including and excluding the ¹P₁ state in the diagonalization and amounts to only 0.4 MHz, completely resolving the difference to the standard cg from Eq. (7). We note that the finite magnetic-moment distribution, included in the Zemach radius of a nucleus, will change the size of the hyperfine constant A but does not affect the center of gravity of the transition.

Systematic uncertainties

In our experiment, the ion velocity and, hence, the laser frequencies in the rest frame of the ions were scanned by changing the voltage potential in the fluorescence detection region (Doppler tuning). The frequencies of the lasers for collinear and anticollinear excitation were stabilized at frequencies that ensure resonant excitation at nearly the same ion velocity and, thus, the same Doppler tuning voltage. The uncertainties of the laser frequencies itself are determined from the statistics of the continuously measured beat signals of the frequency comb and directly considered in the Gaussian error propagation of Eq. (6). Systematic drifts of the laser frequencies are avoided by ensuring a sufficiently high beat signal used for stabilization to the atomic clock reference. Remaining differences δU of the resonance positions were always below 0.5 V. The exact δU is determined from the peak position parameter of the Gaussian lineshape model, which is fitted separately to both the collinear and anticollinear resonance signals. All other parameters of the lineshape model, such as the Gaussian linewidth σ . can also differ between collinear and anticollinear measurements, e.g., due to differences in frequency stability, laser power or laser-beam vibrations. The Gaussian width might differ, even for exact beam overlap, because of slightly different beam sizes and, therefore, additional velocity classes that are addressed by the larger beam. These parameters are, however, uncorrelated with the peak position parameter. To resolve both signals and to get the best signal-to-noise ratio, collinear and anticollinear measurements are recorded only quasisimultaneously, meaning in quick succession. This has the disadvantage that a drifting high-voltage potential in the ion source is directly visible in δU . The main contribution to the drift is a changing electron-beam current in the EBIS. To compensate for this effect, measurements were always taken in the order ac-ca, which eliminates this error entirely as long as the voltage drift is linear. Additionally, the applied acceleration voltage was stabilized with a simple proportional regulator⁷⁷. As a result, no systematic frequency shift due to uncompensated nonlinear voltage drifts was observed.

The largest systematic uncertainty originates from the imperfect alignment of the two laser beams. To make sure both laser beams are interacting with the same ion velocities, the profiles of the laser beams were adjusted to be roughly of the same size in the fluorescence detection region with a radius of 0.7 mm and superposed outside of the beamline at two points in the beam paths, 14 m apart from each other. The maximum displacement of 0.5 mm corresponds to an angle of \leq 0.07 mrad. During a single day of measurements, drifts of the laser-beam positions at the points of alignment, originating e.g., from angular drifts of the Nd:YVO₄ pump lasers or thermal drifts inside the Ti-sapphire cavity, remained below the estimated maximum displacement and were regularly checked and corrected once or twice per day. The ion beam was aligned with the collinear laser using a

Table 3 | Summary of all systematic uncertainties of the transition frequency measurements in ¹³C⁴⁺

Contribution	Symbol	Uncertainty (MHz)
Spatial velocity distribution	$\Delta u_{ m spatial}$	1.72
Laser-/Ion-beam alignment	$\Delta u_{ m angle}$	0.09
Photon recoils	$\Delta u_{ m rec}$	0.41
Laser polarization	$\Delta u_{ m pol}$	0.24
Absolute voltage	$\Delta \nu_{U}$	0.00
Amplification factor	$\Delta u_{\delta U}$	0.00
Total systematic uncertainty	Δυ	1.79

The total systematic uncertainty is given by the geometric sum of all individual uncertainties.

combination of multi-channel plates (MCPs) and phosphor screens in the two beam diagnostic stations, which are 2.6 m apart. Here, a maximum misalignment of 0.62 mrad was estimated. While Dopplerinduced frequency shifts due to the angular deviation are suppressed and amount to ≤ 0.1 MHz, the concomitant spatial separation at the detection region can lead to larger effects due to the horizontal velocity dispersion in the ion beam caused by the 60°-bender at the entrance of the collinear beamline. The frequency shift associated with this effect is directly proportional to the horizontal positional difference of the two laser beams at the points of alignment, including a change in sign at perfect alignment, and was simulated and measured to appear as an additional statistical fluctuation centered around the atomic transition frequency with a standard deviation of 1.72 MHz. Due to the daily realignment of the ion and laser beams over the course of the three-month measurement period, the symmetric distribution of laser alignment configurations was adequately sampled. Additional uncertainties due to the Zeeman effect, photon recoils beyond the considered correction in Eq. (6) and the residual Doppler shift caused by the angular misalignment of the ion- and laser beams are listed in Table 3 and are added in square to yield a total systematic uncertainty of 1.8 MHz. For further details, see^{47,48,78}. Due to the statistical nature of the systematic uncertainties, the total uncertainties of v_i provided in Table 1 are the systematic and statistical uncertainties added in square.

Nuclear Hamiltonians

We employ Hamiltonians with nucleon-nucleon and three-nucleon interactions from chiral effective field theory (EFT), where the full intrinsic Hamiltonian has the form $H = T - T_{cm} + V_{NN} + V_{3N}$ with the total kinetic energy T, the center-of-mass kinetic energy of the A-body nucleus $T_{\rm cm}$, the nucleon-nucleon (NN) potential $V_{\rm NN}$, and the threenucleon (3N) potential V_{3N} . Chiral EFT Hamiltonians are truncated at a finite order in the EFT expansion, making nuclear Hamiltonians intrinsically uncertain. We employ several Hamiltonians that differ in their construction and fit to data to probe this uncertainty. The 1.8/ 2.0(EM), 2.0/2.0(EM), and 2.2/2.0(EM) Hamiltonians are constructed from the N³LO NN potential developed by Entem and Machleidt (EM) in ref. 79 unitarily transformed to the resolution scales $\lambda = 1.8$, 2.0, and 2.2 ħfm⁻¹, respectively, via the similarity renormalization group⁸⁰ and 3N potentials at N²LO with a regulator cutoff of 2.0 ħfm⁻¹ ⁶⁹. The NN potential is fitted to NN scattering data and the deuteron binding energy, and the 3N potentials are fitted to reproduce the binding energy of ³H and the point-proton radius of ⁴He for each of the transformed NN potentials. The names of these Hamiltonians are constructed from the NN resolution scale λ and the 3N cutoff Λ , " $\lambda/\Lambda(EM)$ ", with the "(EM)" indicating the starting NN potential⁷⁹. The N²LO_{sat} Hamiltonian is constructed from N²LO NN and 3N potentials with a regulator cutoff of $\Lambda = 450 \text{ MeV/}c$ and is fitted to NN scattering data, deuteron properties, ground-state energies and charge radii of few-body systems with $A \le 4$, and selected ground-state energies and charge radii for ¹⁴C and ^{16,22,24,25}O⁷⁰, where the fit to medium-mass nuclei helps to improve nuclear matter saturation properties of the

interaction. The ΔN^2LO_{GO} Hamiltonian, developed by the Gothenburg and Oak Ridge groups (GO), is constructed from N²LO NN and 3N potentials with a cutoff of $\Lambda = 2.0 \, h \text{fm}^{-1}$ with the explicit inclusion of Δ isobars in the EFT⁷¹. It is fitted to NN scattering data, properties of fewbody systems with $A \le 4$, and nuclear matter properties, and additionally optimized to reproduce bulk properties of medium-mass nuclei. The family of non-local interactions up to N⁴LO⁷² used in the IM-NCSM are constructed using the NN potentials from ref. 81 up to N⁴LO and 3N interactions at N²LO and N³LO⁸² with non-local regulators of Λ = 500 and 550 MeV/c, where N⁴LO′ indicates a hybrid interaction with NN at N⁴LO and 3N at N³LO. The NN and 3N interactions are consistently unitarily transformed using the similarity renormalization group to a resolution scale of $\alpha = 0.08 \, \text{fm}^4$ (corresponding to $\lambda = 1.88 \, h \text{fm}^{-1}$). The NN interactions are fitted to NN scattering data and deuteron properties, and the 3N interactions are fitted to the groundstate energies of 3H and 16O.

Nuclear structure calculations

Both the VS-IMSRG and the IM-NCSM are variants of the IMSRG^{65,83}, which produces a unitary transformation of the Hamiltonian to solve the Schrödinger equation. This transformation, generally parametrized as $U=\exp(\Omega)$, is normal ordered with respect to a reference state $|\Phi_0\rangle$, allowing it in practice to be truncated at the normal-ordered two-body level. All other operators, in particular charge radius operators, are consistently transformed using the same transformation, allowing for the computation of ground-state expectation values. In this work, nuclear charge radii R_c are determined with R_c

$$R_{\rm c} = \sqrt{\langle R_{\rm p}^2 \rangle + \langle r_{\rm p}^2 \rangle + \frac{N}{Z} \langle r_{\rm n}^2 \rangle + \frac{3\hbar^2}{4m_{\rm p}^2c^2} + \langle r^2 \rangle_{\rm so}}, \tag{10}$$

with the point-proton squared charge radius $\langle R_{\rm p}^2 \rangle$, the proton and $\langle r_{\rm p}^2 \rangle = (0.8409 \, {\rm fm})^2$ squared charge radii $\langle r_{\rm n}^2 \rangle = -0.1155 \, {\rm fm}^{2}{}^{85}$, the relativistic Darwin-Foldy correction $3\hbar^2/4m_{\rm p}^2c^2 = 0.0332 \, {\rm fm}^2$, and the spin-orbit correction $\langle r^2 \rangle_{\rm so}$. Our IM-NCSM calculations neglect spin-orbit charge radius corrections, which contribute $0.0023-0.0033\,\text{fm}^2$ for $^{12}\text{C},\ 0.015-0.025\,\text{fm}^2$ for $^{13}\text{C},\ \text{and}$ 0.0027–0.0045 fm for $\delta R_{\rm c}^{12,13}$ depending on the interaction, well within the assessed uncertainties. We note that in the optimization of the N²LO_{sat} Hamiltonian, a larger proton radius has been used, while here we employ the most recent value reported by the particle data group. This might lead to slightly smaller absolute radii, but will largely cancel in $\delta R_c^{12,13}$. All theoretical nuclear charge radii are compiled in Table 2. The differential and absolute radii are plotted in Figs. 3 and 4, respectively.

The VS-IMSRG^{67,86} transforms the Hamiltonian such that a nucleus-specific valence-space Hamiltonian is decoupled, which can then be diagonalized using standard shell-model techniques. Our VS-IMSRG calculations start from a Hartree-Fock (HF) reference state. In particular, we employ Hartree-Fock single-particle states for states occupied in our reference state. For the remaining states, we employ the perturbatively improved natural orbital (NAT) basis⁸⁷, orthogonalizing the NAT basis with respect to the occupied HF states. We use the VS-IMSRG truncated at the normal-ordered two-body level, the VS-IMSRG(2), to decouple a p-shell valence space. A final diagonalization is performed with KSHELL⁸⁸. Recent developments have made the VS-IMSRG calculations truncated at the normal-ordered three-body level available⁷³, and we explore the effect of the normal-ordered two-body truncation in our calculations by performing VS-IMSRG(3)-N⁷ calculations. This captures induced three-body terms, leading to a more accurate solution of the many-body Schrödinger equation. For the final shell-model diagonalization, we truncate the residual three-body terms of all operators and perform the diagonalization with up to two-body operators.

The IM-NCSM⁶⁸ starts out with a standard NCSM calculation in a small reference space $N_{\text{max}} = 2$, using a natural orbital basis⁸⁹. In a second step, this reference space is decoupled from higher-lying many-body states using the Magnus version of the multi-reference IMSRG truncated at the normal-ordered two-body level. The resulting Hamiltonian and consistently transformed operators are then used in a final NCSM calculation $N_{\text{max}} = 4$ to obtain the relevant observables. The uncertainties due to many-body truncations are probed by an explicit variation of the reference space and the final model-space truncation, as well as a variation of the IMSRG flow parameter. The chiral truncation uncertainties are extracted from the order-by-order variation of the observables through a Bayesian model⁷⁴. For this, we use IM-NCSM calculations for all chiral orders starting at NLO for the aforementioned family of non-local interactions. Note that we apply this uncertainty quantification protocol directly to the radius differences as well, thus exploiting correlations of the radii in the two isotopes.

Data availability

The data sets generated in the experiment and analyzed for the current study are publicly available at https://doi.org/10.48328/tudatalib-1500.

References

- Hofstadter, R. Electron scattering and nuclear structure. Rev. Mod. Phys. 28, 214 (1956).
- Fitch, V. L. & Rainwater, J. Studies of X-rays from Mu-mesonic atoms. Phys. Rev. 92, 789 (1953).
- Borie, E. & Rinker, G. A. The energy levels of muonic atoms. Rev. Mod. Phys. 54, 67 (1982).
- Fricke, G. et al. Nuclear ground state charge radii from electromagnetic interactions. At. Data Nucl. Data Tables 60, 177 (1995).
- Fricke, G. & Heilig, K. Nuclear Charge Radii, in Landolt-Börnstein, Group I: Elementary Particles, Nuclei and Atoms Vol. 20 (Springer, Berlin, Heidelberg, New York, 2004).
- Udem, T. et al. Phase-coherent measurement of the hydrogen 1S-2S transition frequency with an optical frequency interval divider chain. *Phys. Rev. Lett.* 79, 2646 (1997).
- Bernauer, J. C. et al. High-precision determination of the electric and magnetic form factors of the proton. *Phys. Rev. Lett.* 105, 242001 (2010).
- 8. Pohl, R. et al. The size of the proton. Nature 466, 213 (2010).
- Beyer, A. et al. The Rydberg constant and proton size from atomic hydrogen. Science 358, 79 (2017).
- Grinin, A. et al. Two-photon frequency comb spectroscopy of atomic hydrogen. Science 370, 1061 (2020).
- Bezginov, N. et al. A measurement of the atomic hydrogen Lamb shift and the proton charge radius. Science 365, 1007 (2019).
- Fleurbaey, H. et al. New measurement of the 1S-3S transition frequency of hydrogen: contribution to the proton charge radius puzzle. *Phys. Rev. Lett.* 120, 183001 (2018).
- Brandt, A. D. et al. Measurement of the 2S_{1/2}-8D_{5/2} transition in hydrogen. *Phys. Rev. Lett.* 128, 023001 (2022).
- Xiong, W. et al. A small proton charge radius from an electronproton scattering experiment. *Nature* 575, 147 (2019).
- Lin, Y.-H., Hammer, H.-W. & Meißner, U.-G. New insights into the Nucleon's electromagnetic structure. *Phys. Rev. Lett.* 128, 052002 (2022).
- Gao, H. & Vanderhaeghen, M. The proton charge radius. Rev. Mod. Phys. **94**, 015002 (2022).
- Gilman, R. et al. Technical design report for the Paul Scherrer Institute experiment R-12-01.1: studying the proton "radius" puzzle with µp elastic scattering. arXiv https://arxiv.org/abs/1709. 09753 (2017).
- Krauth, J. J. et al. Measuring the α-particle charge radius with muonic helium-4 ions. Nature 589, 527 (2021).

- Schuhmann, K. et al. The helion charge radius from laser spectroscopy of muonic helium-3 ions. Science 388, 854 (2025).
- Li Muli, S. S., Richardson, T. R. & Bacca, S. Revisiting the Helium isotope-shift puzzle with improved uncertainties from nuclear structure corrections. *Phys. Rev. Lett.* 134, 032502 (2025).
- van der Werf, Y. et al. Alpha and helion particle charge radius difference determined from quantum-degenerate helium. Science 388, 850 (2025).
- 22. Qi, X.-Q. Toward resolving the discrepancy in helium-3 and helium-4 nuclear charge radii. *Phys. Rev. Research* **7**, L022020 (2025).
- Pachucki, K., Patkóš, V. & Yerokhin, V. A. Second-order hyperfine correction to H, D, and ³He energy levels. arXiv https://arxiv.org/ abs/2411.05621 (2024).
- 24. Ohayon, B. et al. Towards precision muonic X-ray measurements of charge radii of light nuclei. *Physics* **6**, 206 (2024).
- Sick, I. Precise nuclear radii from electron scattering. Phys. Lett. B 116, 212 (1982).
- Ruckstuhl, W. et al. Precision measurement of the 2p-1s transition in muonic ¹²C: search for new muon-nucleon interactions or accurate determination of the rms nuclear charge radius. *Nucl. Phys. A* 430, 685 (1984).
- 27. Lu, Z.-T. et al. *Colloquium*: laser probing of neutron-rich nuclei in light atoms. *Rev. Mod. Phys.* **85**, 1383 (2013).
- Wheeler, J. A. On the mathematical description of light nuclei by the method of resonating group structure. Phys. Rev. 52, 1107 (1937).
- 29. von Weizsäcker, C. F. Neuere Modellvorstellungen über den Bau der Atomkerne. *Naturwissenschaften* **26**, 209 (1938).
- Kanada-En'yo, Y. & Horiuchi, H. Structure of light unstable nuclei studied with antisymmetrized molecular dynamics. *Prog. Theor. Phys. Suppl.* 142, 205 (2001).
- 31. Ikeda, K., Takigawa, N. & Horiuchi, H. The systematic structure-change into the molecule-like structures in the self-conjugate 4n nuclei. *Prog. Theor. Phys. Suppl.* **E68**, 464 (1968).
- 32. von Oertzen, W., Freer, M. & Kanada En'Yo, Y. Nuclear clusters and nuclear molecules. *Phys. Rep.* **432**, 43 (2006).
- Nörtershäuser, W., Neff, T., Sánchez, R. & Sick, I. Charge radii and ground state structure of lithium isotopes: experiment and theory reexamined. *Phys. Rev. C.* 84, 024307 (2011).
- Krieger, A. et al. Frequency-comb referenced collinear laser spectroscopy of Be⁺ for nuclear structure investigations and many-body QED tests. Appl. Phys. B 123, 15 (2017).
- 35. Maaß, B. et al. Nuclear charge radii of ^{10,11}B. *Phys. Rev. Lett.* **122**, 182501 (2019).
- Hoyle, F. On nuclear reactions occurring in very hot STARS.I. The synthesis of elements from carbon to nickel. Astrophys. J. Suppl. Ser. 1, 121 (1954).
- 37. Neff, T., Feldmeier, H. & Roth, R. Clusters and shell-structure in light nuclei. *AIP Conf. Proc.* **764**, 387 (2005).
- Epelbaum, E., Krebs, H., Lähde, T. A., Lee, D. & Meißner, U.-G. Structure and rotations of the Hoyle state. *Phys. Rev. Lett.* 109, 252501 (2012).
- Freer, M. & Fynbo, H. The Hoyle state in ¹²C. *Prog. Part. Nucl. Phys.* 78, 1 (2014).
- Otsuka, T. et al. α-Clustering in atomic nuclei from first principles with statistical learning and the Hoyle state character. Nat. Commun. 13, 2234 (2022).
- Wallerstein, G. et al. Synthesis of the elements in stars: forty years of progress. Rev. Mod. Phys. 69, 995 (1997).
- 42. Fynbo, H. O. U. et al. Revised rates for the stellar triple- α process from measurement of 12 C nuclear resonances. *Nature* **433**, 136 (2005).
- Jin, S., Roberts, L. F., Austin, S. M. & Schatz, H. Enhanced triple-α reaction reduces proton-rich nucleosynthesis in supernovae. *Nat-ure* 588, 57 (2020).

- Nörtershäuser, W. et al. Nuclear charge radii of ^{7,9,10}Be and the oneneutron halo nucleus ¹¹Be. Phys. Rev. Lett. 102, 062503 (2009).
- Krieger, A. et al. Nuclear charge radius of ¹²Be. *Phys. Rev. Lett.* **108**, 142501 (2012).
- Geithner, W. et al. Masses and charge radii of ¹⁷⁻²²Ne and the twoproton-halo candidate ¹⁷Ne. *Phys. Rev. Lett.* **101**, 252502 (2008).
- 47. Imgram, P., König, K., Maaß, B., Müller, P. & Nörtershäuser, W. Collinear laser spectroscopy of 2 ³S₁→2 ³P_J transitions in heliumlike ¹²C⁴⁺. Phys. Rev. Lett. **131**, 243001 (2023).
- 48. Imgram, P., König, K., Maaß, B., Müller, P. & Nörtershäuser, W. Collinear laser spectroscopy of highly charged ions produced with an electron-beam ion source. *Phys. Rev. A* **108**, 062809 (2023).
- 49. Pohl, R. et al. Laser spectroscopy of muonic deuterium. *Science* **353**, 669 (2016).
- 50. König, K. et al. A new collinear apparatus for laser spectroscopy and applied science (COALA). Rev. Sci. Instrum. 91, 081301 (2020).
- Kramida, A., Ralchenko, Y., Reader, J. & NIST ASD Team. NIST Atomic Spectra Database (ver. 5.10) https://doi.org/10.18434/ T4W30F (2022).
- 52. Johnson, W. R., Cheng, K. T. & Plante, D. R. Hyperfine structure of 2 ³P levels of heliumlike ions. *Phys. Rev. A* **55**, 2728 (1997).
- 53. Nörtershäuser, W. et al. Precision test of many-body QED in the Be^+2p fine structure doublet using short-lived isotopes. *Phys. Rev. Lett.* **115**, 033002 (2015).
- 54. Yerokhin, V. A., Patkóš, V. & Pachucki, K. QED calculations of energy levels of heliumlike ions with 5≤Z≤30. *Phys. Rev. A* **106**, 022815 (2022).
- Heisenberg, J., McCarthy, J. S. & Sick, I. Elastic electron scattering from ¹³C. Nucl. Phys. A 157, 435 (1970).
- de Boer, F. et al. Precision measurement of the 2p-1s transition wavelength in muonic ¹³C. Nucl. Phys. A 444, 589 (1985).
- 57. Roth, R., Neff, T., Hergert, H. & Feldmeier, H. Nuclear structure based on correlated realistic nucleon–nucleon potentials. *Nucl. Phys. A* **745**, 3 (2004).
- Neff, T. & Feldmeier, H. Cluster structures within fermionic molecular dynamics. *Nucl. Phys. A* 738, 357 (2004).
- Chernykh, M., Feldmeier, H., Neff, T., von Neumann-Cosel, P. & Richter, A. Structure of the Hoyle state in ¹²C. *Phys. Rev. Lett.* 98, 032501 (2007).
- 60. Epelbaum, E., Krebs, H., Lee, D. & Meissner, U.-G. Ab initio calculation of the Hoyle state. *Phys. Rev. Lett.* **106**, 192501 (2011).
- 61. Elhatisari, S. et al. Wavefunction matching for solving quantum many-body problems. *Nature* **630**, 59 (2024).
- 62. Hergert, H. A guided tour of ab initio nuclear many-body theory. *Front. Phys.* **8**, 379 (2020).
- 63. Hu, B. et al. Ab initio predictions link the neutron skin of ²⁰⁸Pb to nuclear forces. *Nat. Phys.* **18**, 1196 (2022).
- Hebeler, K. et al. Normal ordering of three-nucleon interactions for ab initio calculations of heavy nuclei. *Phys. Rev. C.* 107, 024310 (2023).
- 65. Hergert, H., Bogner, S. K., Morris, T. D., Schwenk, A. & Tsukiyama, K. The in-medium similarity renormalization group: a novel ab initio method for nuclei. *Phys. Rep.* **621**, 165 (2016).
- Hergert, H. et al. Ab initio multireference in-medium similarity renormalization group calculations of even calcium and nickel isotopes. *Phys. Rev. C.* 90, 041302 (2014).
- 67. Stroberg, S. R. et al. Nucleus-dependent valence-space approach to nuclear structure. *Phys. Rev. Lett.* **118**, 032502 (2017).
- 68. Gebrerufael, E., Vobig, K., Hergert, H. & Roth, R. Ab initio description of open-shell nuclei: merging no-core shell model and in-medium similarity renormalization group. *Phys. Rev. Lett.* **118**, 152503 (2017).
- Hebeler, K., Bogner, S. K., Furnstahl, R. J., Nogga, A. & Schwenk, A. Improved nuclear matter calculations from chiral low-momentum interactions. *Phys. Rev. C.* 83, 031301 (2011).

- 70. Ekström, A. et al. Accurate nuclear radii and binding energies from a chiral interaction. *Phys. Rev. C.* **91**, 051301 (2015).
- Jiang, W. G. et al. Accurate bulk properties of nuclei from A = 2 to ∞ from potentials with ∆ isobars. Phys. Rev. C. 102, 054301 (2020).
- 72. Hüther, T., Vobig, K., Hebeler, K., Machleidt, R. & Roth, R. Family of chiral two- plus three-nucleon interactions for accurate nuclear structure studies. *Phys. Lett. B* **808**, 135651 (2020).
- Heinz, M., Tichai, A., Hoppe, J., Hebeler, K. & Schwenk, A. Inmedium similarity renormalization group with three-body operators. *Phys. Rev. C.* 103, 044318 (2021).
- Melendez, J. A., Furnstahl, R. J., Phillips, D. R., Pratola, M. T. & Wesolowski, S. Quantifying correlated truncation errors in effective field theory. *Phys. Rev. C.* 100, 044001 (2019).
- 75. Virtanen, P. et al. SciPy 1.0: fundamental algorithms for scientific computing in Python. *Nat. Methods* **17**, 261 (2020).
- Stone, N. J. https://inis.iaea.org/search/51052833 Table of recommended nuclear magnetic dipole moments (2019).
- Müller, P., König, K., Imgram, P., Krämer, J. & Nörtershäuser, W. Collinear laser spectroscopy of Ca⁺: solving the field-shift puzzle of the 4s ²S_{1/2}→4p ²P_{1/2,3/2} transitions. *Phys. Rev. Res.* 2, 043351 (2020).
- Müller, P. Laser-spectroscopic determination of the nuclear charge radius of ¹³C, https://doi.org/10.26083/tuprints-00026746 Doctoral thesis (PhD thesis), Technische Universität Darmstadt (2024).
- 79. Entem, D. R. & Machleidt, R. Accurate charge-dependent nucleon-nucleon potential at fourth order of chiral perturbation theory. *Phys. Rev. C.* **68**, 041001 (2003).
- 80. Bogner, S. K., Furnstahl, R. J. & Perry, R. J. Similarity renormalization group for nucleon-nucleon interactions. *Phys. Rev. C.* **75**, 061001 (2007).
- 81. Entem, D. R., Machleidt, R. & Nosyk, Y. High-quality two-nucleon potentials up to fifth order of the chiral expansion. *Phys. Rev. C.* **96**, 024004 (2017).
- Hebeler, K., Krebs, H., Epelbaum, E., Golak, J. & Skibiński, R. Efficient calculation of chiral three-nucleon forces up to N3LO for ab initio studies. *Phys. Rev. C.* 91, 044001 (2015).
- Tsukiyama, K., Bogner, S. K. & Schwenk, A. In-medium similarity renormalization group for nuclei. *Phys. Rev. Lett.* **106**, 222502 (2011).
- 84. Ong, A., Berengut, J. C. & Flambaum, V. V. Effect of spin-orbit nuclear charge density corrections due to the anomalous magnetic moment on halonuclei. *Phys. Rev. C.* **82**, 014320 (2010).
- 85. Workman, R. L. et al. Review of particle physics. *Prog. Theor. Exp. Phys.* **2022**, 083C01 (2022).
- Stroberg, S. R., Hergert, H., Bogner, S. K. & Holt, J. D. Nonempirical interactions for the nuclear shell model: an update. *Annu. Rev. Nucl. Part. Sci.* 69, 307 (2019).
- Hoppe, J., Tichai, A., Heinz, M., Hebeler, K. & Schwenk, A. Natural orbitals for many-body expansion methods. *Phys. Rev. C.* 103, 014321 (2021).
- 88. Shimizu, N., Mizusaki, T., Utsuno, Y. & Tsunoda, Y. Thick-restart block Lanczos method for large-scale shell-model calculations. *Comput. Phys. Commun.* **244**, 372 (2019).
- 89. Tichai, A., Müller, J., Vobig, K. & Roth, R. Natural orbitals for ab initio no-core shell model calculations. *Phys. Rev. C.* **99**, 034321 (2019).
- Cardman, L. S. et al. The charge distribution of ¹²C. Phys. Lett. B 91, 203 (1980).
- 91. Reuter, W., Fricke, G., Merle, K. & Miska, H. Nuclear charge distribution and rms radius of ¹²C from absolute elastic electron scattering measurements. *Phys. Rev. C.* **26**, 806 (1982).
- 92. Offermann, E. A. et al. Energy dependence of the form factor for elastic electron scattering from ¹²C. *Phys. Rev. C.* **44**, 1096 (1991).

 Schaller, L. A. et al. Nuclear charge radii of the carbon isotopes ¹²C, ¹³C and ¹⁴C. Nucl. Phys. A 379, 523 (1982).

Acknowledgements

We acknowledge support by the Deutsche Forschungsgemeinschaft (DFG, German Research Foundation)—Project-ID 279384907—SFB 1245. The experiment (P.I., K.K., B.M., P.M., W.N.) was also supported in part by the BMBF under Contract Nos. 05P19RDFN1 and 05P21RDFNA. P.M. and P.I. acknowledge support from HGS-HIRE. M.H., T.M., and A.S. were supported in part by the European Research Council (ERC) under the European Union's Horizon 2020 research and innovation program (Grant Agreement No. 101020842).

Author contributions

The experiment was planned, prepared and performed by P.I., K.K., B.M., P.M., and W.N. The data analysis was performed by P.M. The theoretical calculations were developed and performed by M.H., T.M., R.R., and A.S. The paper was written by P.M., M.H., T.M., W.N., R.R., and A.S. All authors read and approved the manuscript.

Funding

Open Access funding enabled and organized by Projekt DEAL.

Competing interests

The authors declare no competing interests.

Additional information

Supplementary information The online version contains supplementary material available at https://doi.org/10.1038/s41467-025-60280-9.

Correspondence and requests for materials should be addressed to Patrick Müller or Wilfried Nörtershäuser.

Peer review information *Nature Communications* thanks the anonymous reviewer(s) for their contribution to the peer review of this work. A peer review file is available.

Reprints and permissions information is available at http://www.nature.com/reprints

Publisher's note Springer Nature remains neutral with regard to jurisdictional claims in published maps and institutional affiliations.

Open Access This article is licensed under a Creative Commons Attribution 4.0 International License, which permits use, sharing, adaptation, distribution and reproduction in any medium or format, as long as you give appropriate credit to the original author(s) and the source, provide a link to the Creative Commons licence, and indicate if changes were made. The images or other third party material in this article are included in the article's Creative Commons licence, unless indicated otherwise in a credit line to the material. If material is not included in the article's Creative Commons licence and your intended use is not permitted by statutory regulation or exceeds the permitted use, you will need to obtain permission directly from the copyright holder. To view a copy of this licence, visit http://creativecommons.org/licenses/by/4.0/.

© The Author(s) 2025